Journal of Bone and Mineral Metabolism (2022) 40:839–852
https://doi.org/10.1007/s00774-022-01354-2

ORIGINAL ARTICLE

Deletion of *Tfam* in *Prx1-Cre* expressing limb mesenchyme results in spontaneous bone fractures

Hiroki Yoshioka[1] · Shingo Komura[1] · Norishige Kuramitsu[1] · Atsushi Goto[1] · Tomoka Hasegawa[2] · Norio Amizuka[2] · Takuya Ishimoto[3] · Ryosuke Ozasa[3] · Takayoshi Nakano[3] · Yuuki Imai[4] · Haruhiko Akiyama[1]

Received: 8 March 2022 / Accepted: 21 June 2022 / Published online: 10 August 2022

Abstract

Introduction Osteoblasts require substantial amounts of energy to synthesize the bone matrix and coordinate skeleton mineralization. This study analyzed the effects of mitochondrial dysfunction on bone formation, nano-organization of collagen and apatite, and the resultant mechanical function in mouse limbs.

Materials and methods Limb mesenchyme-specific *Tfam* knockout (*Tfam*$^{f/f}$;*Prx1-Cre*: *Tfam*-cKO) mice were analyzed morphologically and histologically, and gene expressions in the limb bones were assessed by in situ hybridization, qPCR, and RNA sequencing (RNA-seq). Moreover, we analyzed the mitochondrial function of osteoblasts in *Tfam*-cKO mice using mitochondrial membrane potential assay and transmission electron microscopy (TEM). We investigated the pathogenesis of spontaneous bone fractures using immunohistochemical analysis, TEM, birefringence analyzer, microbeam X-ray diffractometer and nanoindentation.

Results Forelimbs in *Tfam*-cKO mice were significantly shortened from birth, and spontaneous fractures occurred after birth, resulting in severe limb deformities. Histological and RNA-seq analyses showed that bone hypoplasia with a decrease in matrix mineralization was apparent, and the expression of type I collagen and osteocalcin was decreased in osteoblasts of *Tfam*-cKO mice, although *Runx2* expression was unchanged. Decreased type I collagen deposition and mineralization in the matrix of limb bones in *Tfam*-cKO mice were associated with marked mitochondrial dysfunction. *Tfam*-cKO mice bone showed a significantly lower Young's modulus and hardness due to poor apatite orientation which is resulted from decreased osteocalcin expression.

Conclusion Mice with limb mesenchyme-specific *Tfam* deletions exhibited spontaneous limb bone fractures, resulting in severe limb deformities. Bone fragility was caused by poor apatite orientation owing to impaired osteoblast differentiation and maturation.

Keywords Mitochondrial dysfunction · Osteoblast differentiation · Spontaneous bone fracture · Type I collagen · Apatite orientation

Introduction

Mitochondrial aerobic energy production is the primary source of intracellular adenosine triphosphate (ATP). Intracellular ATP levels reflect cell viability, growth and morphology [1, 2]. Moreover, partial ATP depletion, which amounts to approximately 10–65% of the control, results in duration-dependent induction of apoptosis, morphological changes, and plasma membrane alternations [3]. The mitochondrial respiratory chain located in the mitochondrial inner membrane generates a majority of the cellular ATP via oxidative phosphorylation [4]. Mitochondrial DNA (mtDNA) encodes 13 respiratory chain subunits that

✉ Haruhiko Akiyama
hakiyama@gifu-u.ac.jp

[1] Department of Orthopaedic Surgery, Graduate School of Medicine, Gifu University, 1-1 Yanagido, Gifu 501-1194, Japan

[2] Department of Developmental Biology of Hard Tissue, Graduate School of Dental Medicine, Hokkaido University, Sapporo, Japan

[3] Division of Materials and Manufacturing Science, Graduate School of Engineering, Osaka University, Osaka, Japan

[4] Division of Integrative Pathophysiology, Proteo-Science Center, Ehime University, Toon, Ehime, Japan

are required for mitochondrial biogenesis and normal cellular functions [5, 6]. Mitochondrial transcription factor A (Tfam), a nuclear DNA-encoded protein, is necessary for mtDNA maintenance, promotes transcription, and regulates mtDNA replication [7–9]. *Tfam* disruption causes severe mtDNA depletion, resulting in decreased ATP production due to the abolition of oxidative phosphorylation [1, 10].

Osteoblasts are derived from mesenchymal stem cells (MSCs). *Runx2* expressing pre-osteoblasts differentiate into type I collagen-expressing osteoblasts. They subsequently mature, synthesize bone matrix proteins, and coordinate the mineralization of bone tissues [11]. Owing to their unique functions, the synthetic phase of mature osteoblasts requires substantial amounts of energy [12]. Mature osteoblasts, which contain abundant granular endoplasmic reticulum (ER), possess moderate numbers of ovoid mitochondria with abundant cristae and increase ATP production and mitochondrial membrane potential during their differentiation and maturation [13, 14]. Mature osteoblasts produce matrix proteins, including type I collagen, osteocalcin (Oc), and calcium phosphate mineral apatite, to mineralize bones [11]. The crystallographic *c*-axis of apatite aligns almost parallel to the collagen fiber direction during normal mineralization [15], resulting in the formation of an oriented nanocomposite. Thus, the stronger direction of apatite and collagen co-align in one direction, making the bone stiff and tough in the collagen/apatite-oriented direction [16, 17]. Recent investigations have revealed that the preferential orientation of collagen/apatite is a potential explanatory factor of bone fragility in some pathologic bones [18–20].

Although the osteoblast maturation process, which requires substantial ATP, may be involved in mitochondrial energy production, few studies have analyzed mitochondrial function in osteogenesis and bone formation *in vivo* [21]. In this study, we analyzed the effect of mitochondrial dysfunction on bone formation following the limb-mesenchyme-specific deletion of *Tfam*.

Materials and methods

Mice

The experimental design and study protocols were approved by the Animal Experiment Committee of Gifu University and were performed in compliance with the Animal Research: Reporting of in Vivo Experimental (ARRIVE) guidelines. *Tfam* flox mice ($Tfam^{f/f}$) [10] were crossed with *Prx1-Cre* transgenic mice [22] to generate $Tfam^{f/f}$; *Prx1-Cre* (*Tfam*-cKO) mice), and $Tfam^{f/f}$ mice were used as controls. All experiments were conducted using mice with a complete C57BL/6 background. Genotyping for *Tfam* and *Cre* transgenes was performed using polymerase chain reaction (PCR), as previously described [10].

Histological analysis

Alcian blue and alizarin red staining of the skeleton was performed as previously described [23]. For histological analysis, embryos and newborn mice were fixed with 4% paraformaldehyde (FUJIFILM Wako Pure Chemical Corporation, Osaka, Japan) at 4 °C for 24 h. Postnatal samples were decalcified with ethylene-diamine-tetra-acetic acid (EDTA) (G-Chelate Mild, GenoStuff, Tokyo, Japan) for 3–7 days before fixation. Serial Sects. (5 µm) were stained with hematoxylin and eosin (H&E) (FUJIFILM Wako), von Kossa staining using Calcium Stain Kit (Cosmo Bio, Tokyo, Japan). Alkaline phosphatase (ALP) was detected using the TRAP/ALP Stain Kit (FUJIFILM Wako), and type I and type III collagens were detected using the Picrosirius Red Stain Kit (Cosmo Bio) according to the manufacturer's instructions. RNA in situ hybridization using ^{35}S labeling of RNA probes was performed as previously described [24–26]. Images of hybridization signals were captured with a red filter and superimposed with blue fluorescence images of cell nuclei stained with Hoechst 33,258 dye (Sigma-Aldrich, St. Louis, MO, USA). Immunohistochemical staining was performed using an EnVision Detection Kit (Dako, Santa Clara, CA, USA). The following antibodies were used: anti-collagen I (ab270993, Abcam, Cambridge, UK), anti-osteocalcin (ab93876, Abcam), Anti-Ki67 (ab16667, Abcam), and Alexa Fluor 488 secondary antibodies (Invitrogen, Waltham, MA, USA). Terminal deoxynucleotidyl transferase dUTP nick end labeling (TUNEL) analysis was performed using the In Situ Cell Death Detection Kit, AP (Sigma-Aldrich) following the manufacturer's instructions.

Radiographic analysis

Radiographic examination was performed with a Faxitron cabinet X-ray system (Model 43855D, Faxitron X-Ray LLC, Lincolnshire, IL, USA) using an energy of 26 kV and exposure time of 10 s, as previously reported [23]. Forelimbs excised from postnatal 3-month-old mice were scanned using ScanXmate micro-computed tomography (micro-CT) (Model D150SS270, Comscantecno, Kanagawa, Japan), using an energy of 60 kV and a resolution of 18.0 µm/pixel (Kureha Special Laboratory, Fukushima, Japan).

Cell culture

MC3T3-E1 cells (Riken Cell Bank, Ibaraki, Japan) were seeded at $4 \times 10^4/cm^2$ in minimum essential medium α (Gibco, Waltham, MA, USA) supplemented with 10% fetal bovine serum and 1% penicillin–streptomycin (FUJIFILM

Wako) and cultured in a 37 °C incubator with 5% CO_2 for 24 h. Osteoblast differentiation was induced using 50 µg/mL ascorbic acid (Nacalai Tesque, Kyoto, Japan) and 10 mM β-glycerophosphate (FUJIFILM Wako) (Osteoblast differentiation media). Primary osteoblasts were obtained from the humerus of *Tfam*-cKO and control mice and cultured as previously reported [27]. Rotenone (Sigma-Aldrich), an inhibitor of mitochondrial aerobic energy metabolism, was added 48 h before harvest. si*Tfam* and non-targeting siRNA (Horizon Discovery, Cambridge, UK) as controls (siCTL) were transfected with Lipofectamine® RNAiMAX (Invitrogen) according to the manufacturer's instructions.

Cell proliferation analysis

Cell proliferation of MC3T3-E1 cells in 96-well microplates cultured for three days was assessed using the Cell Proliferation ELISA, BrdU (colorimetric) (Roche, Basel, Switzerland), following the manufacturer's instructions. The absorbance of the samples was measured at a wavelength of 450 nm using Microplate Reader (Model 680, Bio-Rad Laboratories, Hercules, CA, USA). The relative absorbance was calculated as a ratio to that of the control samples.

RNA and DNA isolation and quantitative real-time PCR

The humerus at postnatal 5–6 days was excised and the bone marrow was thoroughly flushed out with phosphate buffer saline as previously described [27]. Total RNA and DNA content were isolated from humerus and MC3T3-E1 cells using RNeasy or DNeasy (Qiagen, Venlo, Netherlands), and RNA was reverse-transcribed using a High-Capacity cDNA Reverse Transcription Kit (Applied Biosystems, Foster City, MA, USA) according to the manufacturer's instructions. Quantitative real-time PCR (qPCR) of complementary DNA (cDNA) and total extracted DNA was performed using TB Green® Premix Ex Taq™ II (Tli RNaseH Plus) (Takara Bio, Shiga, Japan). β-actin expression and nuclear DNA (nDNA) copy number served as controls for RNA expression and mitochondrial DNA copy number, respectively. Changes in gene expression were quantified using the ΔΔCT method. Primer sequences used for qPCR are listed in Table 1.

Analysis of oxygen consumption rate (OCR)

Cellular OCR was analyzed using a Cell Mito Stress Test Kit (Agilent Technologies, Santa Clara, CA, USA), according to the manufacturer's instructions. Briefly, the cells were seeded onto an XFp Cell Culture Miniplate (Agilent Technologies) at 3×10^4/80 µL/well and incubated overnight. OCR measurements were performed with 1 µM oligomycin, 2 µM FCCP, 0.5 µM rotenone, and antimycin A using a Seahorse XFp Extracellular Flux Analyzer (Agilent Technologies).

Analysis of ATP content in the humerus

The ATP content in the humerus was measured using ATPlite (Perkin Elmer, Waltham, MA, USA) according to the manufacturer's instructions.

Proteomic analysis

For proteomic analysis (Medical Proteoscope, Kanagawa, Japan), paraffin blocks of humerus obtained from postnatal day 6 *Tfam*-cKO and control mice were sectioned into 10 µm thick sections for laser microdissection. The sections

Table 1 Primers in real-time PCR

	Forward (5′→3′)	Reverse (5′→3′)
Tfam	TCTGTCTCCTGAGGAAAAGCAG	TCACACTTCGACGGATGAGATC
β-actin	CTAAGGCCAACCGTGAAAAGATGAC	TCTCCGGAGTCCATCACAATGCCTG
Col1a1	GCTCCTCTTAGGGGCCACT	CCACGTCTCACCATTGGGG
Oc	AAGCAGGAGGGCAATAAGGTAG	TCTGATAGCTCGTCACAAGCAG
Runx2	AATTGCAGGCTTCGTGGTTG	TGTGTTCCTAGGTTCTCCAAGC
Mmp13	CTTTGGCTTAGAGGTGACTGG	AGGCACTCCACATCTTGGTTT
mt-Co1	ATGCAGGAGCATCAGTAGACCTAAC	GAGTTTGATACTGTGTTATGGCTGG
mt-Nd1	TTACTTCTGCCAGCCTGACCCATAG	GCTGCGTATTCTACGTTAAACCCTG
mt-Atp6	GGAGCCGTAATTACAGGCTTCCGAC	GCCGGACTGCTAATGCCATTGGTTG
mt-Atp8	AAAGTCTCATCACAAACATTCCCAC	GGGGTAATGAATGAGGCAAATAGAT
Sod1	GCGGTGAACCAGTTGTGTTGTC	CAGTCACATTGCCCAGGTCTCC
Sod2	ATGTTACAACTCAGGTCGCTCTTC	TGATAGCCTCCAGCAACTCTCC
Sod3	CTCTTGGGAGAGCCTGACA	GCCAGTAGCAAGCCGTAGAA
mtDNA	CCTATCACCCTTGCCATCAT	GAGGCTGTTGCTTGTGTGAC
nDNA	ATGGAAAGCCTGCCATCATG	TCCTTGTTGTTCAGCATCAC

were deparaffinized and stained with hematoxylin to determine the cortical bone area. Microdissection was performed using LMD7000 (Leica, Wetzlar, Germany), and total areas of 6.64 mm^2 and 6.95 mm^2 were transferred into microtubes from the section of *Tfam*-cKO and the control mice, respectively. Proteins were extracted and digested with trypsin using Liquid Tissue (Expression Pathology Inc., Rockville, MD, USA) according to the manufacturer's instructions. The digested peptide samples (2 µL) were analyzed by liquid chromatography–tandem mass spectrometry (LC–MS/MS) using an Ultimate 3000 RSLCnano (Thermo Fisher Scientific, Waltham, MA, USA) and a Q Exactive Orbitrap mass spectrometer (Thermo Fisher Scientific), as previously described [28]. The MS/MS data obtained were searched against mouse protein sequences (17,013 entries) in the Swiss-Prot database (January 2019) and the amino acid sequences of protein contaminants (116 entries) in the Global Proteome Machine Organization using MASCOT software, version 2.5 (Matrix Science, London, United Kingdom). We used a 1% false discovery rate as the cut-off for peptide and protein identification. All data were deposited into jPOST (identification number JPST001511) and Proteome XChange (PXID identification number PXD031994).

Transmission electron microscope (TEM) analysis

The humeral tissues were pretreated for TEM observations as previously described [29]. Briefly, specimens were immersed in a mixture containing 2% paraformaldehyde and 2.5% glutaraldehyde diluted in 0.067 M cacodylate buffer (pH 7.4). After fixation, some specimens were decalcified for 1–2 weeks with 5% EDTA and subsequently post-fixed with 1 % osmium tetraoxide in 0.1 M cacodylate buffer for 4 h at 4°C, dehydrated in ascending acetone solutions, and embedded in epoxy resin (Epon 812, Berkshire, UK). The remaining specimens were undecalcified and post-fixed with osmium tetraoxide for epoxy resin embedding. Ultrathin sections of the decalcified specimens were prepared using an ultramicrotome and were stained with uranyl acetate, lead citrate, and tannate before TEM observations (Hitachi H-7100, Hitachi Co. Ltd, Tokyo, Japan) at 80 kV [30]. Unstained sections of the undecalcified specimens were prepared and observed (Tokai Electron Microscopy Inc., Aichi, Japan). The specimens were ultra-thin-sectioned at 90 nm with a diamond knife using an ultramicrotome (Ultracut UCT; Leica), and the sections were mounted on copper grids. The grids were observed under a TEM (JEM-1400Plus; JEOL Ltd., Tokyo, Japan) at 100 kV.

Mitochondrial membrane potential assay (JC-1)

The MitoPT® JC-1 Assay kit (Immunochemistry Technologies, Bloomington, MN, USA) was used to detect the mitochondrial membrane potential according to the manufacturer's instructions.

Next-generation sequencing (NGS) analysis

The total extracted RNA from the humeral bone of postnatal day 6 mice was subjected to RNA sequencing (RNA-seq) as previously described [31–33]. The integrity of isolated RNA was verified using a 2100 Bioanalyzer (Agilent Technologies). RNA samples with an integrity number > 8 were normalized to 100 ng/mL before further analysis. RNA-seq libraries were prepared using the NEBNext Ultra II Directional RNA Library Prep Kit for Illumina, NEBNext Poly (A) mRNA Magnetic Isolation Module, and NEBNext Multiplex Oligos for Illumina (New England Biolabs, MA, USA) according to the manufacturer's instructions. Each library was sequenced on the MiSeq system with the MiSeq Reagent kit v3 150 cycles (Illumina, San Diego, CA, USA) using 75 base pair ends. Differentially expressed genes were determined using an exact test after normalization. The genes with expression levels that were significantly increased or decreased in *Tfam*-cKO mice by more than two-fold compared with the control mice were extracted for further analyses. Pathway analysis was performed using DAVID Bioinformatics Resources (https://david.ncifcrf.gov/), as described previously [34]. RNA-seq data were deposited in the Gene Expression Omnibus database under the accession code GSE196628.

Analysis of apatite *c*-axis orientation by microbeam X-ray diffractometer

The apatite *c*-axis orientation of the humerus was analyzed using a microbeam X-ray diffractometer (µXRD) system (R-Axis BQ, Rigaku, Tokyo, Japan), which was equipped with a transmission-type optical system and an imaging plate (storage phosphors) (FUJIFILM, Tokyo, Japan), as previously described [18]. The measurements were performed at seven points along the bone axis with a regular interval of 1/10th of the bone length, and point 5 corresponded to the bone longitudinal center. The incident X-ray was focused on a beam spot 300 µm in diameter by a double-pinhole metal collimator and radiated in the anteroposterior axis; diffraction data were collected for 1200 s. The degree of preferential orientation of the apatite *c*-axis was assessed as the ratio of the relative intensity of the (002) diffraction peak to that of the (310) peak in the X-ray profile. The intensity ratio was calculated from the upper and lower parts of the Debye ring, and averaged. Detected values > 0.8 indicated the presence of anisotropic apatite *c*-axis orientation in the bone longitudinal axis.

Analysis of collagen orientation by birefringence analyzer

Collagen orientation of the left humerus was analyzed using a two-dimensional birefringence measurement system WPA-micro (Photonic Lattice, Miyagi, Japan) attached to an upright microscope (BX60; Olympus, Tokyo, Japan), as previously described [18, 19]. Specimens were sagittally cut into 10 µm-thick sections, and deparaffinized sections were imaged using a 20 × objective lens. For a quantitative comparison of collagen orientation, the orientation order parameter, which takes a value ranging from -1 (collagen perfectly aligned perpendicular to the longitudinal axis) to 1 (collagen perfectly aligned parallel to the longitudinal axis), was calculated as previously described [35]. Data were acquired from the anterior and posterior cortices at the center of the bone length and the results were averaged.

Analysis of Young's modulus using nanoindentation

Young's modulus was analyzed using a nanoindentation system (ENT-1100; Elionix, Tokyo, Japan) as previously described [18]. Embedded humeral bone specimens were cut transversely at the longitudinal center, and their surfaces were ground and mirror-polished. Load–depth measurements were carried out according to the established conditions [36]. Young's modulus and hardness were determined using the method described by Oliver and Pharr [37]. Five indentations were created on the anterior and posterior cortices and the results were averaged.

Statistical analysis

All data were analyzed using GraphPad Prism software (GraphPad, San Diego, CA, USA). Data are expressed as the mean ± standard deviation. The experiments were repeated at least thrice. Statistical significance was analyzed using unpaired *t* test, one-way analysis of variance, and Tukey's test as a post hoc test. p value < 0.05 was considered statistically significant ($*p < 0.05$, $**p < 0.01$).

Results

Conditional deletion of *Tfam* in *Prx1* expressing limb mesenchyme caused spontaneous bone fractures and severe skeletal deformities of the limbs

To investigate the mitochondrial function during bone formation in vivo, we created *Prx1* expressing limb mesenchyme-specific *Tfam* knockout (*Tfam*-cKO) mice. *Tfam*-cKO mice were born at the expected Mendelian frequencies. Deletion of *Tfam* genes was confirmed in the limb mesenchyme of *Tfam*-cKO mice (Figure S1a), and the expression of *Tfam* was significantly reduced in the humerus of *Tfam*-cKO mice compared with that of the control mice (Figure S1b). The forelimbs of *Tfam*-cKO mice were markedly shortened from birth which is the same phenotypes reported previously [38], and the shortening of the radius was more significant than that of the humerus (Fig. 1a–c). Surprisingly, *Tfam*-cKO mice forelimbs presented spontaneous bone fractures around the olecranon within a few days and 1 week after birth (Fig. 1b, d). These bone phenotypes progressed with aging and finally reached severe skeletal deformities (Fig. 1a, b, d). The appearance of joints in the forelimbs of *Tfam*-cKO mice did not change morphologically until fractures occurred (Fig. 1b, d).

Osteoblast differentiation and maturation were inhibited in *Tfam*-cKO mice

Next, we performed histological and gene expression analyses to investigate osteogenesis in the *Tfam*-cKO mice. Mesenchymal condensation in the limb bud and chondrocyte differentiation in the growth plate were comparable between *Tfam*-cKO and control mice at embryonic 13.5 days (Fig. 2a); moreover, the overall structure of the developing growth plate was also comparable in *Tfam*-cKO mice reported previously [38] (Fig. 2a). The formation of the first ossification center was clearly delayed at embryonic 16.5 days in *Tfam*-cKO mice, and the hypoplasia of bone trabeculae became apparent at 0 and 14 days after birth (Fig. 2a). *Tfam*-cKO mice exhibited decreased expression of *collagen type I alpha 1* (*Col1a1*) in the first ossification center and *Oc* in the bone collar compared to control mice. In contrast, the expression of *Runx2*, which is expressed in preosteoblasts and differentiated osteoblasts, did not change (Fig. 2b). Indeed, qPCR analyses showed that *Col1a1* and *Oc* expression in the humerus derived from *Tfam*-cKO mice was significantly decreased compared to that in the control mice, and the expression of *Runx2* was unchanged (Fig. 2c). As shown in Fig. 2d, *Tfam*-cKO mice showed decreased mineralization in the bone collar and cortical bone by von Kossa staining with decreased ALP activity. Moreover, the number of Ki67 positive cells in the cancellous bones was lower in *Tfam*-cKO mice (Figure S2a), and the number of TUNEL-positive cells did not differ between the two mice ($p = 0.844$ in hypertrophic zone and $p = 0.585$ in trabecular bone) (Figure S2b, S2c). Additionally, the expression of *Mmp13* and the number of TRACP-positive cells, which are osteoclast markers, were similar in both mice (Fig. 2b–d).

The expressions of *Col1a1* and *Oc* genes were downregulated in the humerus of *Tfam*-cKO mice

Global gene expression in the humerus obtained from *Tfam*-cKO and control mice was analyzed by NGS. The

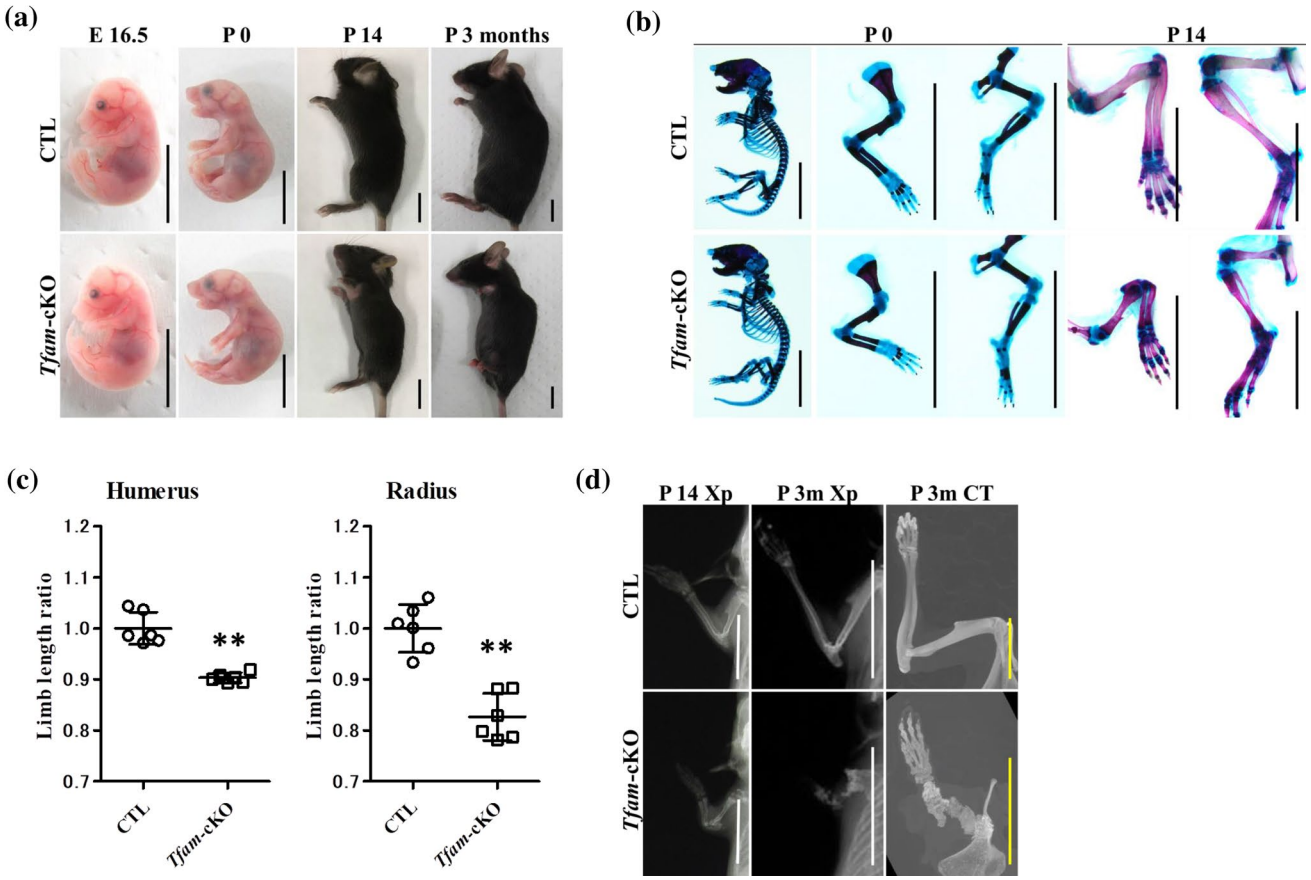

Fig. 1 Skeletal phenotypes in *Tfam*-cKO mice. **a** Gross appearance of embryonic 16.5 days, newborn, postnatal 14 days and 3 months. The bars denote 10 mm. **b** Skeletal preparation of whole mount and limbs at newborn and postnatal 14 days. The bars denote 10 mm. **c** Limb length ratio is calculated in humerus and radius at birth. The mean values ± SD and each value plot of total bone length ratio in forelimbs are shown (6 biological replicates). **d** Radiographs of forelimbs at postnatal 14 days and 3 months. The bars denote 10 mm. Micro-computed tomography images at postnatal 3 months. The bars denote 5 mm

expression levels of 929 genes were downregulated more than two-fold in the *Tfam*-cKO mice. Among the 929 genes, 279 were significantly differentially expressed between the two groups ($q < 0.05$). Additionally, 140 genes with expression values higher than the median value of the control were selected (Fig. 3a, b). *Col1a1* and *Oc* were included in these genes (Fig. 3a). Next, we performed Gene Ontology (GO) analyses of these 140 genes using the DAVID Bioinformatics Resources. Enriched functional annotation clustering of keywords (Up keywords category), such as "Calcium," "Collagen," "Extracellular matrix (ECM)" and "Metal-binding", was confirmed (Fig. 3c). Moreover, "Extracellular space," "Extracellular region," "Proteinaceous ECM," "Collagen type I trimer," and "collagen trimer" were enriched in GO terms of Cellular Component category (Fig. 3d). In GO terms of Molecular Function category, "Collagen binding," "structural constituent of bone" and "ECM structural constituent" were enriched (Fig. 3e).

Bone fragility of *Tfam*-cKO mice was through inhibition of type I collagen deposition and mineralization of bone matrix in association with impairment of apatite orientation

Following NGS analysis, we focused on type I collagen, which is produced by osteoblasts, as the main collagen-composed bone matrix [12]. We performed immunohistochemical analysis, TEM observations, and orientation analysis to detect the protein expression level of type I collagen, deposition of collagen fibers, and collagen orientation properties, respectively. Proteomic analysis and histochemical staining revealed that type I collagen expression and deposition were markedly reduced in the humerus, particularly in the cortical bone of *Tfam*-cKO mice, compared with that in control mice (Fig. 4a, S3a). Furthermore, type I collagen fibers in the cortex stained by Picrosirius Red and in the bone matrix directly under osteoblasts shown in TEM observations were thinner and less

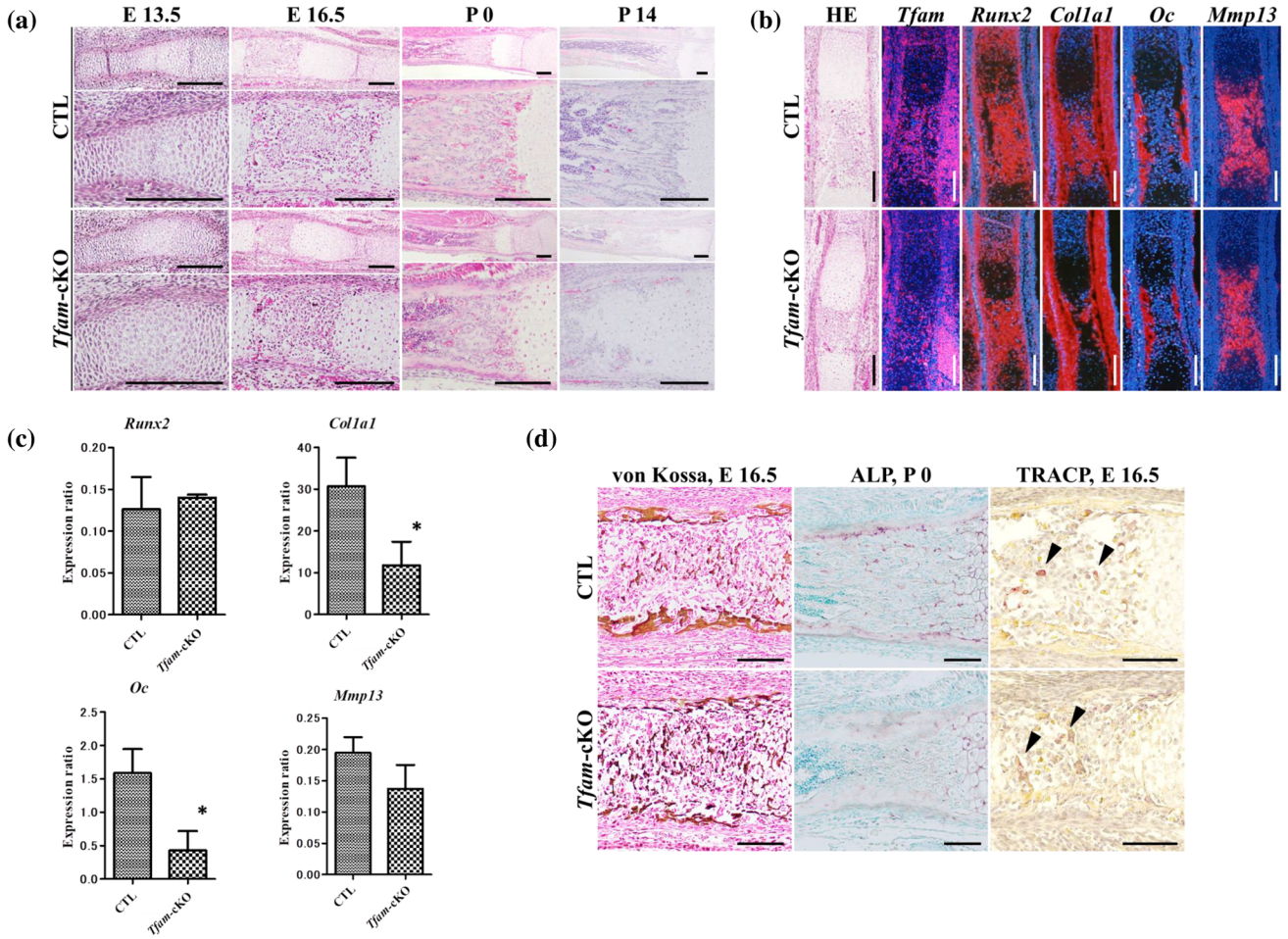

Fig. 2 Histological analyses and gene expression of osteoblast and osteoclast markers in *Tfam*-cKO mice. **a** Hematoxylin–eosin (HE) staining at embryonic 16.5 days, newborn and postnatal 14 days. The bars denote 200 µm. **b** In situ hybridization to assess expression of osteoblast and osteoclast markers in ulna at embryonic 16.5 days. The bars denote 200 µm. **c** Expression of osteoblast and osteoclast markers in humerus at postnatal 6 days by qPCR. The mean values ± SD of expression ratio to β-actin are shown (3 biological replicates, 3 technical replicates). **d** von Kossa staining at embryonic 16.5 days, ALP staining at newborn and TRACP staining (arrowheads indicate TRACP-positive cells) at embryonic 16.5 days. The bars denote 100 µm

dense in *Tfam*-cKO mice than in control mice (Fig. 4a, b). In addition, collagen orientation at the humerus in *Tfam*-cKO mice was lower than that in control mice (Fig. 4c). Next, we focused on apatite orientation, which is involved in bone strength. Histochemical staining showed that Oc expression decreased in the humerus of *Tfam*-cKO mice (Fig. 4d). TEM observations showed that calcified spherical bodies in the bone matrix directly under osteoblasts were decreased in *Tfam*-cKO mice (Fig. 4e). Interestingly, orientation analysis showed that the intensity ratio of apatite *c*-axis orientation at the humeral diaphyseal center in *Tfam*-cKO mice was significantly lower than that in control mice. Although the values were much greater than 0.8 in control mice, the values in *Tfam*-cKO mice were near 0.8, indicating an isotropic orientation (Fig. 4f). This result revealed that the anisotropic apatite *c*-axis orientation was lost along the longitudinal axis of the humerus in *Tfam*-cKO mice. Moreover, analysis of the mechanical properties of the humerus in *Tfam*-cKO mice showed that Young's modulus and hardness at the diaphyseal center of the humerus were significantly lower than those in the control mice (Fig. 4g). Finally, we performed a multiple regression analysis to calculate the factor coefficient of orientational dominance in Young's modulus and hardness. The factor scores of apatite orientation for both parameters were significantly higher than those of collagen orientation were (Fig. 4h), indicating that bone fragility of limbs in *Tfam*-cKO mice was affected by impairment of mineralization rather than that of collagen fibrillogenesis and nano-organization.

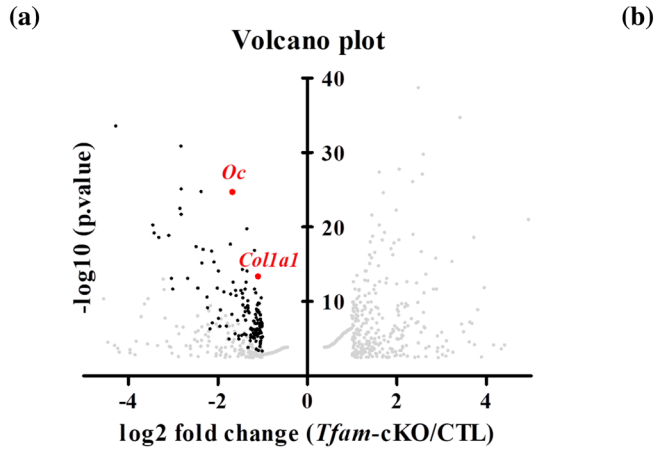

(b)

Log2 fold change (Tfam-cKO/CTL)	<-1	-1~1	1<
All genes (%)	929 (4.0)	21457 (91.6)	1034 (4.4)
Genes with q < 0.05 (%)	279 (1.2)	-	294 (1.3)
Higher than median value (%)	140 (0.60)	-	147 (0.63)

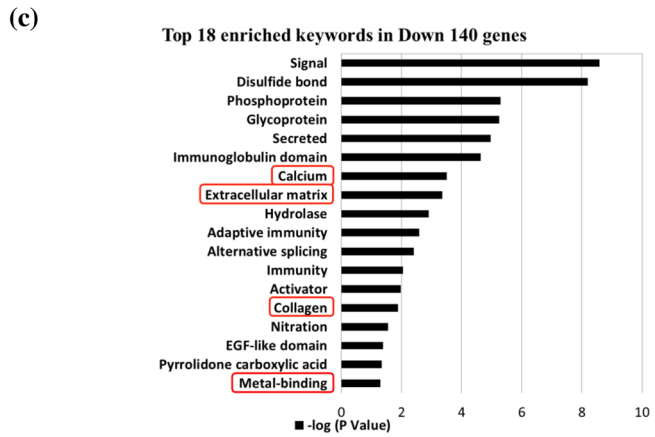

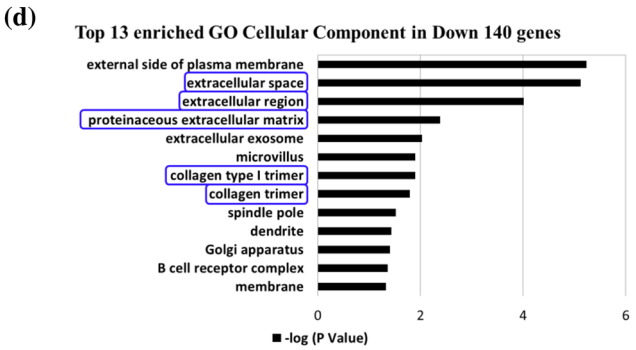

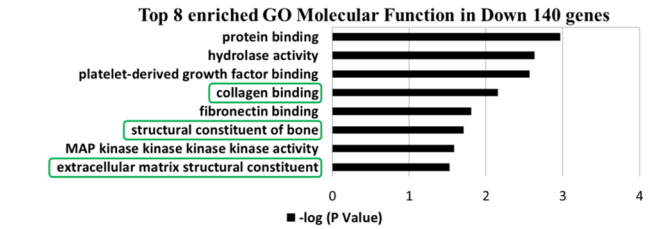

Fig. 3 NGS analysis of RNA sequence in humeral bone of postnatal day 6 *Tfam*-cKO mice. **a** Volcano plot for RNA sequencing data obtained from humerus at postnatal 6 days (3 biological replicates). All of dots indicate genes that are significantly ($q < 0.05$) and differentially expressed in *Tfam*-cKO mice by more than two-fold, of which black dots indicate genes that express higher than median value of the control genes expression. *Col1a1*: collagen type I alpha 1, *Oc*: osteocalcin. **b** The table summarizes the number and percentage of differentially expressed (upper row), significantly expressed genes (middle row) and expressed higher than median value of the control genes expression (lower row). **c** Gene Ontology (GO) analysis using the DAVID Bioinformatics Resources. Functional annotation clustering of keywords among the GO terms for 140 genes that are significantly downregulated in *Tfam*-cKO mice compared with the control mice. **d** The enriched GO Cellular Component in 144 genes significantly downregulated in *Tfam*-cKO mice. **e** The enriched GO Molecular Function in 144 genes significantly downregulated in *Tfam*-cKO mice

mtDNA maintenance and aerobic energy production were impaired in the osteoblasts of *Tfam*-cKO mice

To confirm mitochondrial dysfunction in the osteoblasts of *Tfam*-cKO mice, mitochondrial membrane potential was analyzed using JC-1 assay. Red fluorescence, which indicated high mitochondrial membrane potential, was decreased in the osteoblasts derived from the humerus of *Tfam*-cKO mice compared with those of the control mice (Fig. 5a). The contents of mtDNA and ATPs in the humerus of *Tfam*-cKO mice were markedly reduced compared to those of the control humerus (Fig. 5b, c). The expression of mitochondrial aerobic energy metabolism-associated genes, such as *mt-Co1*, *mt-Nd1*, *mt-Atp6*, and *mt-Atp8*, was significantly decreased in the humerus of *Tfam*-cKO mice (Fig. 5d), whereas the genes associated with protection against reactive oxidative species (ROS) did not change (Figure S4a). TEM observations clearly showed morphological changes in the mitochondria and ER (Fig. 5e). Enlarged mitochondria with disarrayed cristae were apparent in osteoblasts of the humerus of *Tfam*-cKO newborn mice, and the change became more prominent four days after birth. Moreover, there was an abundance of granular ERs in osteoblasts of control mice, whereas those in *Tfam*-cKO mice were sparsely located (Fig. 5e).

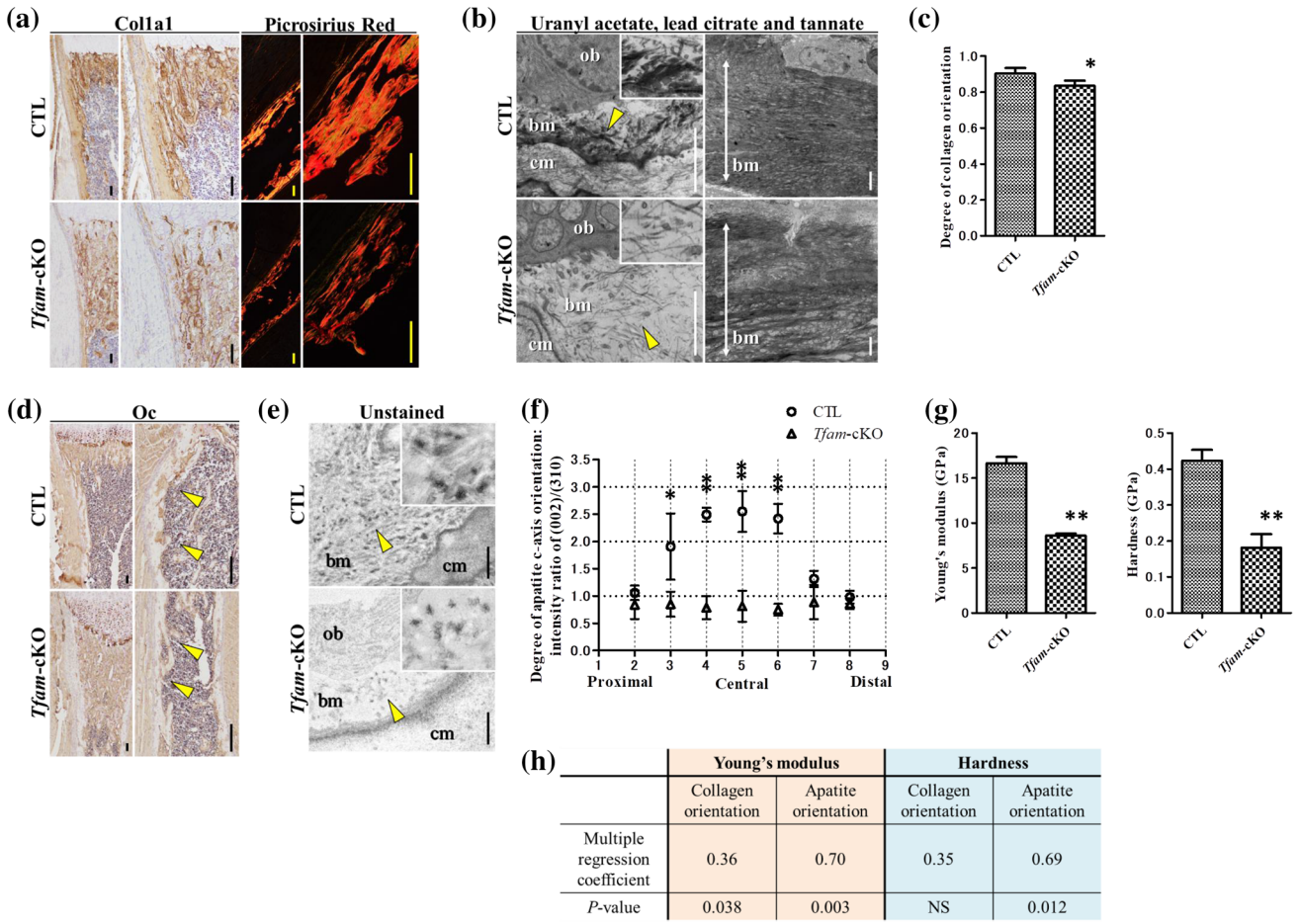

(h)

	Young's modulus		Hardness	
	Collagen orientation	Apatite orientation	Collagen orientation	Apatite orientation
Multiple regression coefficient	0.36	0.70	0.35	0.69
P-value	0.038	0.003	NS	0.012

Fig. 4 Analyses of collagen fibrillogenesis, apatite deposition, and mechanical property in *Tfam*-cKO mice. **a** Immunohistochemical staining of type I collagen and Picrosirius Red staining to assess collagen deposition and fibrillogenesis in proximal humerus at postnatal 6 days. The bars denote 100 µm. **b** Images obtained from TEM observations. Sections are stained with uranyl acetate, lead citrate and tannate. Yellow arrowheads indicate collagen fibers at bone matrix directly under osteoblasts. White double-headed arrows indicate area of collagen fiber fascicle at bone matrix. ob: osteoblast, bm: bone matrix, cm: cartilage matrix, The bars denote 2 µm. **c** Collagen orientation of humerus at postnatal 6 days is analyzed by birefringence analyzer. The mean values ± SD of the orientation order parameter are calculated (4 biological replicates). **d** Immunohistochemical staining of osteocalcin (Oc) in humerus at postnatal 6 days. Yellow arrowheads indicate Oc positive area. The bars denote 100 µm. **e** Images obtained from TEM observations. Yellow arrowheads indicate calcified spherical bodies in bone matrix. ob: osteoblast, bm: bone matrix, cm: cartilage matrix. The bars denote 2 µm. **f** Apatite c-axis orientation of humerus at postnatal 6 days is analyzed by microbeam X-ray diffractometer. The mean values ± SD of intensity ratio are shown (4 biological replicates). **g** Young's modulus of humerus at postnatal 6 days are analyzed by nanoindentation. The mean values ± SD of Young's modulus (GPa) and hardness (GPa) are shown (4 biological replicates). **h** Multiple regression analysis to calculate the factor coefficient of orientational dominance in Young's modulus and hardness. As the value of coefficient is higher, it indicates the dominance is stronger

Inhibition of mitochondrial energy production by *Tfam* knockdown or rotenone hampered osteoblast proliferation and differentiation in vitro

To confirm whether inhibition of mitochondrial function hampered osteoblast proliferation and differentiation *in vitro*, preosteoblast-like MC3T3-E1 cells were cultured in osteoblast differentiation media and treated with si*Tfam* (si*Tfam* group) or non-targeting siRNA as a control (siCTL group). The knockdown efficiency of si*Tfam* is shown in Figure 6a. The expression of *Col1a1*, *Oc,* and mtDNA in the si*Tfam* group was significantly decreased compared to that in the siCTL group (Figure 6b). Cell proliferation was significantly reduced in the si*Tfam* group (Figure 6c). Moreover, the basal OCR, maximal respiration, and mitochondrial ATP production were significantly reduced in the si*Tfam* group (Figure 6d, e). These *in vitro* results represented the gene expression and mitochondrial function of osteoblasts in *Tfam*-cKO mice *in vivo*. Next, MC3T3-E1 cells were cultured with rotenone, an inhibitor of mitochondrial aerobic energy metabolism. The expression of *Col1a1* was significantly decreased by rotenone in a dose-dependent manner

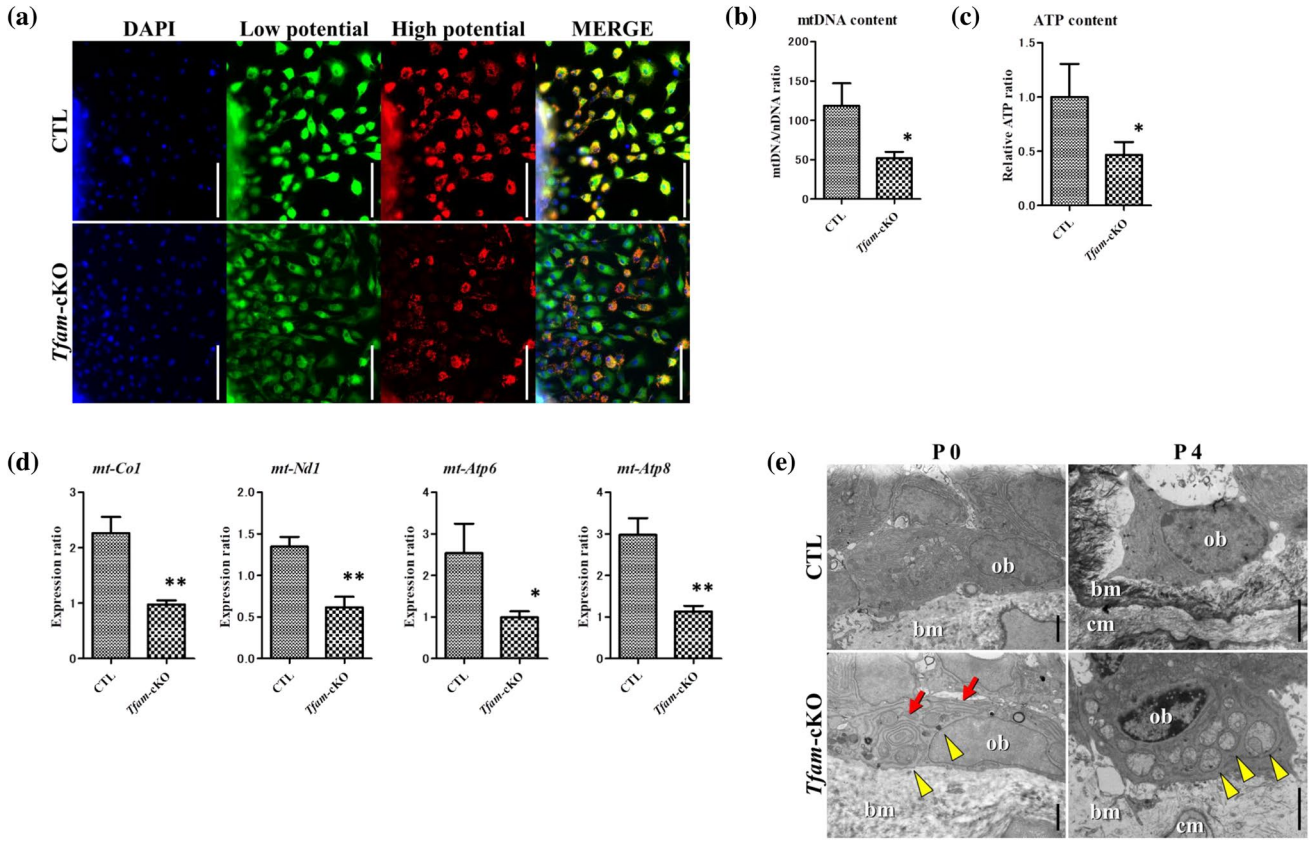

Fig. 5 Analysis of mitochondrial function and morphology in *Tfam*-cKO mice. **a** Mitochondrial membrane potential in osteoblasts derived from humerus of postnatal 6 days mice. Green color indicates low potential and red color indicates high potential. The bars denote 100 µm. **b** mtDNA content in humerus at postnatal 6 days by qPCR. Nuclear DNA (nDNA) served as control. The mean values ± SD of mtDNA ratio to nDNA are shown (3 biological replicates, 3 technical replicates). **c** ATP content in humerus at postnatal 6 days by chemiluminescence assay. The mean values ± SD of relative intensity ratio to the control are shown (3 biological replicates, 3 technical replicates). **d** Expression of genes associated with mitochondrial aerobic energy metabolism in humerus at postnatal 6 days by qPCR. The mean values ± SD of expression ratio to β-actin are shown (3 biological replicates, 3 technical replicates). **e** Images obtained from TEM observations. Yellow arrowheads indicate mitochondria and red arrows indicate rough ERs. ob: osteoblast, bm: bone matrix, cm: cartilage matrix, The bars denote 2 µm

(Figure 6f). However, *Oc* expression decreased slightly only at a high dose of rotenone (Figure 6f). Intracellular ATP levels and cell proliferation were significantly decreased by rotenone in a dose-dependent manner, with no change in mtDNA content (Figure 6g–i).

Discussion

Previous *in vitro* studies have investigated the effects of energy production on osteoblast differentiation and function during bone formation. Osteoblast differentiation depends on a metabolic shift from glycolysis in the cytosol of MSCs and osteogenic progenitors to oxidative phosphorylation (OxPhos) in the mitochondria of osteoblasts [39, 40]. The activity of OxPhos increases during osteoblast differentiation with increasing mitochondrial ATP production [41]. Inhibition of the mitochondrial respiratory chain suppresses osteoblast maturation with decreasing expression of type I collagen [42]. Thus, they supposed that mitochondrial ATP production was critical for osteoblast differentiation and function. Recently, Dobson et al. reported a role for mitochondrial function in osteoblast differentiation during bone formation *in vivo* [21]. Accelerated mtDNA mutation by knockout of mtDNA polymerase gamma (*PolgA*) accelerates bone loss due to reduced osteoblast population densities, increased osteoclast population densities, and increased bone resorption by osteoclasts in association with mitochondrial respiratory chain deficiency. Moreover, they also inhibited matrix mineralization *in vivo*. Our study analyzed the impact of mitochondrial dysfunction on bone formation following limb–mesenchyme-specific deletion of *Tfam* genes. Similar to the findings from *PolgA* mutant mice [21], *Tfam*-cKO mice exhibited impaired osteoblast proliferation, differentiation, and function with decreased ALP activity, type I collagen and osteocalcin production, and matrix

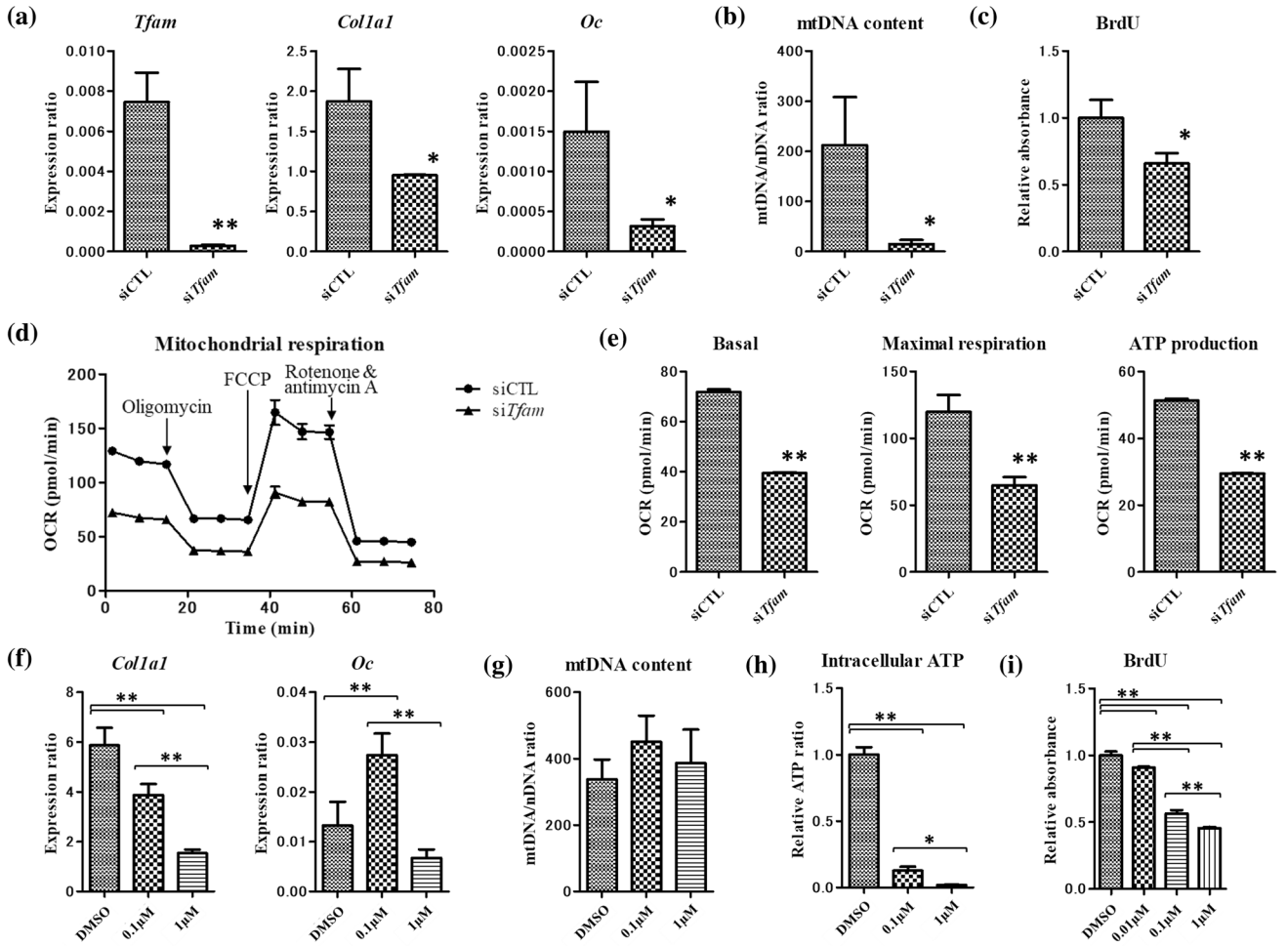

Fig. 6 Effects of *Tfam* knockdown or rotenone in osteoblast-like MC3T3-E1 cells. **a** Expression of *Tfam* gene and osteoblast markers by qPCR with siRNA. si*Tfam* or non-targeting siRNA as control (siCTL). Cells are harvested at 3 days after transfection. The mean values ± SD of expression ratio to β-actin are shown (3 biological replicates, 3 technical replicates). **b** mtDNA contents are assessed by qPCR at 6 days after transfection. The mean values ± SD of mtDNA ratio to nuclear DNA (nDNA) are shown (3 biological replicates, 3 technical replicates). **c** Cell proliferation analysis by BrdU at 2 days after transfection. The mean values ± SD of relative absorbance ratio to dimethyl sulfoxide (DMSO) are shown (3 biological replicates, 3 technical replicates). **d** Oxygen consumption ratio (OCR) are analyzed at 48 h after transfection of si*Tfam* or siCTL. The OCR changes over time are measured and the mean values ± SD are shown (3 biological replicates, 3 technical replicates). **e** Basal OCR, maximal respiration, and mitochondrial ATP production are calculated. The mean values ± SD are shown (3 biological replicates, 3 technical replicates). **f** Expression of osteoblast markers by qPCR after administration of rotenone. Rotenone or DMSO as control is added for 48 h before harvested. The mean values ± SD of expression ratio to β-actin are shown (3 biological replicates, 3 technical replicates). **g** mtDNA contents are assessed by qPCR at 48 h after administration of rotenone. The mean values ± SD of mtDNA ratio to nDNA are shown (3 biological replicates, 3 technical replicates). **h** Intracellular ATP is assessed by chemiluminescence assay at 48 h after administration of rotenone. The mean values ± SD of relative ATP ratio to DMSO are shown (3 biological replicates, 3 technical replicates). **i** Cell proliferation is analyzed by BrdU at 48 h after administration of rotenone. The mean values ± SD of relative absorbance ratio to DMSO are shown (3 biological replicates, 3 technical replicates)

mineralization due to mitochondrial dysfunction. However, *Tfam*-cKO mice exhibited severe spontaneous bone fractures after birth, whereas, in contrast, the *PolgA* mutant mice showed an age-related loss of bone, a phenotype which is weaker compared with that in *Tfam*-cKO mice. In addition, the osteoclast population density was assumed unchanged in *Tfam*-cKO mice. These findings raise the possibility that Tfam and PolgA may have different functions other than the maintenance of mtDNA during bone formation.

Bone is composed of collagen fibrils filled with apatite mineral crystallite. Bone quality includes a wide range of compositional factors, such as collagen content, mineral crystallinity, and collagen/apatite alignment, which are related to bone strength [43]. ATP induces mineralization by serving as a phosphate source for mineral deposition [44]. Our study showed that not only poor collagen fibrillogenesis due to decreased expression and matrix deposition of type I collagen but also decreased matrix mineralization resulted in

bone fragility in *Tf*am-cKO mice. Non-collagenous proteins, such as Oc, are also important for bone nano-structure and mechanical property [45]. Moriishi et al. reported that Oc is required for bone quality and strength by adjusting the alignment of biological apatite *c*-axis parallel to the collagen fibrils [46]. Our study showed that the expression of the Oc gene and protein was decreased. The degree of collagen orientation was significantly lower in *Tf*am-cKO mice than in control mice. However, it was still a strong preferential orientation along the humerus longitudinal axis. Nevertheless, the orientation of the apatite *c*-axis was completely disordered in *Tf*am-cKO mice, and the orientation relationship between collagen and apatite *c*-axis seen in normal bone was disrupted due to the reduced expression of Oc. Mineralization was also impaired with a decrease in calcified spherical bodies in the bones of *Tf*am-cKO mice. Furthermore, multiple regression analysis showed that the factor scores of apatite *c*-axis orientation for Young's modulus and hardness were significantly higher than those of collagen orientation. Thus, the deterioration of apatite orientation had a more critical effect on bone fragility than collagen orientation in *Tf*am-cKO mice.

Mitochondria are not only the main source of energy production, but also regulators of protection against ROS and cell death via apoptosis [47, 48]. Increased ROS levels with upregulation of aerobic mitochondrial metabolism during osteoblast differentiation were prevented by superoxide dismutase and catalase [47]. In *Tfam*-cKO mice, TUNEL-positive cells in cancellous bones were not changed compared to those in control mice. These findings suggest that ROS and cell death do not contribute to bone fragility in *Tf*am-cKO mice.

Ca^{2+} regulation is important for bone matrix mineralization. Previous findings suggest that mitochondrial ATP production may be important for mineralization due to Ca^{2+} supplied from the ER [48]. Ca^{2+} levels in the ER are maintained by the energy-consuming pumping activity of Ca^{2+}-ATPases located in the sarco/endoplasmic reticulum (SERCA), and the lumen of the ER is considered a major intracellular Ca^{2+} storage site that is connected to mitochondria-associated membranes [48, 49]. Lysosomes directly contact the mitochondria and subsequently transport Ca^{2+} to the extracellular space as calcium-containing micro-vesicles [50, 51]. Our study showed that calcified spherical bodies in the bone matrix directly under osteoblasts were decreased and granular ERs in osteoblasts were sparsely located in *Tfam*-cKO mice. We also identified that *ATP2A3*, which is a SERCA gene, was downregulated by RNA-seq (shown in the database). These results suggest Tfam is involved in Ca^{2+} storage in osteoblasts and bone matrix mineralization. However, we did not find out the changes in Ca^{2+} content within mitochondria or ERs in osteoblasts of *Tfam*-cKO mice (data not shown); therefore, further investigations are required to reveal the association between Ca^{2+} storage in mitochondria and ERs, and mineralization in the bone matrix of *Tfam*-cKO mice.

Our study found that both mitochondrial dysfunction by *Tfam* knockdown *in vitro* and selective inhibition of mitochondrial energy production by rotenone markedly decreased the levels of intracellular ATP. In both conditions, the levels of extracellular lactate were increased (data not shown), suggesting that the cells in our *in vitro* study survive through compensatory stimulation of glycolysis at least for 48 hours after their treatment. *Tfam* knockdown also decreased *Col1a1* and *Oc* expression, whereas rotenone administration slightly decreased *Oc* expression. The previous study showed that Oc expression of zebrafish larvae in the group of rotenone treatment was lower than in the control group. It causes oxidative stress, thus increased ROS, which inhibit bone growth [52]. In contrast, our study showed that downregulation of *Tfam* expression significantly decreased *Oc* expression without change of *Sod* expression, suggesting that impairment of bone formation by *Tfam* deletion is caused not only by mitochondrial ATP deficiency, but by unknown mechanisms behind decreased *Oc* expression in *Tfam* deficiency. Further investigations are needed to clarify the molecular mechanisms of *Oc* gene expression by *Tfam*.

In conclusion, mitochondrial dysfunction caused by the deletion of *Tfam* genes in limb mesenchyme results in spontaneous bone fractures and leads to severe limb deformities. These bone phenotypes were caused by a decrease in type I collagen production and mineralization due to the impediment of osteoblast differentiation and function, mainly through inhibition of mitochondrial energy production. Furthermore, the deterioration of apatite orientation has a marked effect on bone strength beyond collagen fibrillogenesis under mitochondrial dysfunction in osteoblasts, through the decreased expression of Oc.

Supplementary Information The online version contains supplementary material available at https://doi.org/10.1007/s00774-022-01354-2.

Acknowledgements We thank L. Nils-Göran, T. Miyazaki and Y. Nakamichi for gifting the mice. We thank M. Hirosawa, K. Kondo, and M. Miwa for technical assistance. Our research was supported by the Japan Society for the Promotion of Science KAKENHI (JP18H02922).

Author contributions HY, SK and HA proposed the research project, designed and performed experiments, and wrote the manuscript. NK, AG, TH, TI, RO and YI performed experiments. NA and TN provided technical guidance.

Declarations

Conflict of interest None.

Ethical approval The experimental design and study protocols were approved by theAnimal Experiment Committee of Gifu University and

were performed in compliance with the Animal Research: Reporting of in Vivo Experimental (ARRIVE) guidelines.

References

1. Jeng JY, Yeh TS, Lee JW, Lin SH, Fong TH, Hsieh RH (2008) Maintenance of mitochondrial DNA copy number and expression are essential for preservation of mitochondrial function and cell growth. J Cell Biochem 103:347–357. https://doi.org/10.1002/jcb.21625
2. Yi CH, Pan H, Seebacher J, Jang IH, Hyberts SG et al (2011) Metabolic regulation of protein N-alpha-acetylation by Bcl-xL promotes cell survival. Cell 146:607–620. https://doi.org/10.1016/j.cell.2011.06.050
3. Feldenberg LR, Thevananther S, del Rio M, de Leon M, Devarajan P (1999) Partial ATP depletion induces Fas- and caspase-mediated apoptosis in MDCK cells. Am J Physiol 276:F837–F846. https://doi.org/10.1152/ajprenal.1999.276.6.F837
4. Sörensen L, Ekstrand M, Silva JP, Lindqvist E, Xu B, Rustin P, Olson L, Larsson NG (2001) Late-onset corticohippocampal neurodepletion attributable to catastrophic failure of oxidative phosphorylation in MILON mice. J Neurosci 21:8082–8090. https://doi.org/10.1523/jneurosci.21-20-08082.2001
5. Larsson NG, Clayton DA (1995) Molecular genetic aspects of human mitochondrial disorders. Annu Rev Genet 29:151–178. https://doi.org/10.1146/annurev.ge.29.120195.001055
6. Gaspari M, Larsson NG, Gustafsson CM (2004) The transcription machinery in mammalian mitochondria. Biochim Biophys Acta 1659:148–152. https://doi.org/10.1016/j.bbabio.2004.10.003
7. Parisi MA, Clayton DA (1991) Similarity of human mitochondrial transcription factor 1 to high mobility group proteins. Science 252:965–969. https://doi.org/10.1126/science.2035027
8. Dairaghi DJ, Shadel GS, Clayton DA (1995) Addition of a 29 residue carboxyl-terminal tail converts a simple HMG box-containing protein into a transcriptional activator. J Mol Biol 249:11–28. https://doi.org/10.1006/jmbi.1995.9889
9. Ekstrand MI, Falkenberg M, Rantanen A, Park CB, Gaspari M, Hultenby K, Rustin P, Gustafsson CM, Larsson NG (2004) Mitochondrial transcription factor A regulates mtDNA copy number in mammals. Hum Mol Genet 13:935–944. https://doi.org/10.1093/hmg/ddh109
10. Larsson NG, Wang J, Wilhelmsson H, Oldfors A, Rustin P, Lewandoski M, Barsh GS, Clayton DA (1998) Mitochondrial transcription factor A is necessary for mtDNA maintenance and embryogenesis in mice. Nat Genet 18:231–236. https://doi.org/10.1038/ng0398-231
11. Eriksen EF (2010) Cellular mechanisms of bone remodeling. Rev Endocr Metab Disord 11:219–227. https://doi.org/10.1007/s11154-010-9153-1
12. Dirckx N, Moorer MC, Clemens TL, Riddle RC (2019) The role of osteoblasts in energy homeostasis. Nat Rev Endocrinol 15:651–665. https://doi.org/10.1038/s41574-019-0246-y
13. Dudley HR, Spiro D (1961) The fine structure of bone cells. J Biophys Biochem Cytol 11:627–649. https://doi.org/10.1083/jcb.11.3.627
14. Komarova SV, Ataullakhanov FI, Globus RK (2000) Bioenergetics and mitochondrial transmembrane potential during differentiation of cultured osteoblasts. Am J Physiol Cell Physiol 279:C1220–C1229. https://doi.org/10.1152/ajpcell.2000.279.4.C1220
15. Landis WJ (1995) The strength of a calcified tissue depends in part on the molecular structure and organization of its constituent mineral crystals in their organic matrix. Bone 16:533–544. https://doi.org/10.1016/8756-3282(95)00076-p
16. Nakano T, Kaibara K, Tabata Y, Nagata N, Enomoto S, Marukawa E, Umakoshi Y (2002) Unique alignment and texture of biological apatite crystallites in typical calcified tissues analyzed by microbeam x-ray diffractometer system. Bone 31:479–487. https://doi.org/10.1016/S8756-3282(02)00850-5
17. Ishimoto T, Nakano T, Umakoshi Y, Yamamoto M, Tabata Y (2013) Degree of biological apatite c-axis orientation rather than bone mineral density controls mechanical function in bone regenerated using recombinant bone morphogenetic protein-2. J Bone Miner Res 28:1170–1179. https://doi.org/10.1002/jbmr.1825
18. Ishimoto T, Sato B, Lee JW, Nakano T (2017) Co-deteriorations of anisotropic extracellular matrix arrangement and intrinsic mechanical property in c-src deficient osteopetrotic mouse femur. Bone 103:216–223. https://doi.org/10.1016/j.bone.2017.06.023
19. Sekita A, Matsugaki A, Ishimoto T, Nakano T (2017) Synchronous disruption of anisotropic arrangement of the osteocyte network and collagen/apatite in melanoma bone metastasis. J Struct Biol 197:260–270. https://doi.org/10.1016/j.jsb.2016.12.003
20. Ozasa R, Matsugaki A, Ishimoto T, Kamura S, Yoshida H, Magi M, Matsumoto Y, Sakuraba K, Fujimura K, Miyahara H, Nakano T (2022) Bone fragility via degradation of bone quality featured by collagen/apatite micro-arrangement in human rheumatic arthritis. Bone 155:116261. https://doi.org/10.1016/j.bone.2021.116261
21. Dobson PF, Dennis EP, Hipps D, Reeve A, Laude A, Bradshaw C, Stamp C, Smith A, Deehan DJ, Turnbull DM, Greaves LC (2020) Mitochondrial dysfunction impairs osteogenesis, increases osteoclast activity, and accelerates age related bone loss. Sci Rep 10:11643. https://doi.org/10.1038/s41598-020-68566-2
22. Logan M, Martin JF, Nagy A, Lobe C, Olson EN, Tabin CJ (2002) Expression of Cre Recombinase in the developing mouse limb bud driven by a Prxl enhancer. Genesis 33:77–80. https://doi.org/10.1002/gene.10092
23. Kawashima K, Ogawa H, Komura S, Ishihara T, Yamaguchi Y, Akiyama H, Matsumoto K (2020) Heparan sulfate deficiency leads to hypertrophic chondrocytes by increasing bone morphogenetic protein signaling. Osteoarthr Cartil 28:1459–1470. https://doi.org/10.1016/j.joca.2020.08.003
24. Nakanishi R, Akiyama H, Kimura H, Otsuki B, Shimizu M, Tsuboyama T, Nakamura T (2008) Osteoblast-targeted expression of Sfrp4 in mice results in low bone mass (in eng). J Bone Miner Res 23:271–277. https://doi.org/10.1359/jbmr.071007
25. Lee K, Deeds JD, Segre GV (1995) Expression of parathyroid hormone-related peptide and its receptor messenger ribonucleic acids during fetal development of rats. Endocrinology 136:453–463. https://doi.org/10.1210/endo.136.2.7835276
26. Akiyama H, Chaboissier MC, Martin JF, Schedl A, de Crombrugghe B (2002) The transcription factor Sox9 has essential roles in successive steps of the chondrocyte differentiation pathway and is required for expression of Sox5 and Sox6. Genes Dev 16:2813–2828. https://doi.org/10.1101/gad.1017802
27. Bakker AD, Klein-Nulend J (2012) Osteoblast isolation from murine calvaria and long bones. Methods Mol Biol 816:19–29. https://doi.org/10.1007/978-1-61779-415-5_2
28. Sugahara S, Kume S, Chin-Kanasaki M, Tomita I, Yasuda-Yamahara M, Yamahara K, Takeda N, Osawa N, Yanagita M, Araki SI, Maegawa H (2019) Protein O-GlcNAcylation is essential for the maintenance of renal energy homeostasis and function via lipolysis during fasting and diabetes. J Am Soc Nephrol 30:962–978. https://doi.org/10.1681/ASN.2018090950
29. Hasegawa T, Yamamoto T, Sakai S, Miyamoto Y, Hongo H, Qiu Z, Abe M, Takeda S, Oda K, de Freitas PHL, Li M, Endo K, Amizuka N (2019) Histological effects of the combined administration of eldecalcitol and a parathyroid hormone in the metaphyseal trabeculae of ovariectomized rats. J Histochem Cytochem 67:169–184. https://doi.org/10.1369/0022155418806865

30. Hasegawa T, Endo T, Tsuchiya E, Kudo A, Shen Z, Moritani Y, Abe M, Yamamoto T, Hongo H, Tsuboi K, Yoshida T, Nagai T, Khadiza N, Yokoyama A, Luiz de Freitas PH, Li M, Amizuka N (2017) Biological application of focus ion beam-scanning electron microscopy (FIB-SEM) to the imaging of cartilaginous fibrils and osteoblastic cytoplasmic processes. J Oral Biosci 59:55–62. https://doi.org/10.1016/j.job.2016.11.004
31. Yamashita M, Inoue K, Saeki N, Ideta-Otsuka M, Yanagihara Y, Sawada Y, Sakakibara I, Lee J, Ichikawa K, Kamei Y, Iimura T, Igarashi K, Takada Y, Imai Y (2018) Uhrf1 is indispensable for normal limb growth by regulating chondrocyte differentiation through specific gene expression. Development. https://doi.org/10.1242/dev.157412
32. Iio H, Kikugawa T, Sawada Y, Sakai H, Yoshida S, Yanagihara Y, Ikedo A, Saeki N, Fukada SI, Saika T, Imai Y (2021) DNA maintenance methylation enzyme Dnmt1 in satellite cells is essential for muscle regeneration. Biochem Biophys Res Commun 534:79–85. https://doi.org/10.1016/j.bbrc.2020.11.116
33. Sakakibara I, Yanagihara Y, Himori K, Yamada T, Sakai H, Sawada Y, Takahashi H, Saeki N, Hirakawa H, Yokoyama A, Fukada SI, Sawasaki T, Imai Y (2021) Myofiber androgen receptor increases muscle strength mediated by a skeletal muscle splicing variant of Mylk4. iScience 24:102303. https://doi.org/10.1016/j.isci.2021.102303
34. da Huang W, Sherman BT, Lempicki RA (2009) Systematic and integrative analysis of large gene lists using DAVID bioinformatics resources. Nat Protoc 4:44–57. https://doi.org/10.1038/nprot.2008.211
35. Umeno A, Kotani H, Iwasaka M, Ueno S (2001) Quantification of adherent cell orientation and morphology under strong magnetic fields. IEEE Trans Magn 37:2909–2911
36. Ishimoto T, Nakano T, Yamamoto M, Tabata Y (2011) Biomechanical evaluation of regenerating long bone by nanoindentation. J Mater Sci Mater Med 22:969–976. https://doi.org/10.1007/s10856-011-4266-y
37. Oliver WC, Pharr GM (1992) An improved technique for determining hardness and elastic modulus using load and displacement sensing indentation experiments. J Mater Res 7:1564–1583. https://doi.org/10.1557/JMR.1992.1564
38. Yao Q, Khan MP, Merceron C, LaGory EL, Tata Z, Mangiavini L, Hu J, Vemulapalli K, Chandel NS, Giaccia AJ, Schipani E (2019) Suppressing mitochondrial respiration is critical for hypoxia tolerance in the fetal growth plate. Dev Cell 49:748–63.e7. https://doi.org/10.1016/j.devcel.2019.04.029
39. Hsu YC, Wu YT, Yu TH, Wei YH (2016) Mitochondria in mesenchymal stem cell biology and cell therapy: from cellular differentiation to mitochondrial transfer. Semin Cell Dev Biol 52:119–131. https://doi.org/10.1016/j.semcdb.2016.02.011
40. Zheng CX, Sui BD, Qiu XY, Hu CH, Jin Y (2020) Mitochondrial regulation of stem cells in bone homeostasis. Trends Mol Med 26:89–104. https://doi.org/10.1016/j.molmed.2019.04.008
41. Shum LC, White NS, Mills BN, Bentley KL, Eliseev RA (2016) Energy metabolism in mesenchymal stem cells during osteogenic differentiation. Stem Cells Dev 25:114–122. https://doi.org/10.1089/scd.2015.0193
42. Yeh PS, Chen JT, Cherng YG, Yang ST, Tai YT, Chen RM (2020) Methylpiperidinopyrazole attenuates estrogen-induced mitochondrial energy production and subsequent osteoblast maturation via an estrogen receptor alpha-dependent mechanism. Molecules. https://doi.org/10.3390/molecules25122876
43. Burr DB (2019) Changes in bone matrix properties with aging. Bone 120:85–93. https://doi.org/10.1016/j.bone.2018.10.010
44. Nakano Y, Addison WN, Kaartinen MT (2007) ATP-mediated mineralization of MC3T3-E1 osteoblast cultures. Bone 41:549–561. https://doi.org/10.1016/j.bone.2007.06.011
45. Sroga GE, Vashishth D (2012) Effects of bone matrix proteins on fracture and fragility in osteoporosis. Curr Osteoporos Rep 10:141–150. https://doi.org/10.1007/s11914-012-0103-6
46. Moriishi T, Ozasa R, Ishimoto T, Nakano T, Hasegawa T, Miyazaki T, Liu W, Fukuyama R, Wang Y, Komori H, Qin X, Amizuka N, Komori T (2020) Osteocalcin is necessary for the alignment of apatite crystallites, but not glucose metabolism, testosterone synthesis, or muscle mass. PLoS Genet 16:e1008586. https://doi.org/10.1371/journal.pgen.1008586
47. Chen CT, Shih YR, Kuo TK, Lee OK, Wei YH (2008) Coordinated changes of mitochondrial biogenesis and antioxidant enzymes during osteogenic differentiation of human mesenchymal stem cells. Stem Cells 26:960–968. https://doi.org/10.1634/stemcells.2007-0509
48. Rimessi A, Giorgi C, Pinton P, Rizzuto R (2008) The versatility of mitochondrial calcium signals: from stimulation of cell metabolism to induction of cell death. Biochim Biophys Acta 1777:808–816. https://doi.org/10.1016/j.bbabio.2008.05.449
49. Marchi S, Patergnani S, Missiroli S, Morciano G, Rimessi A, Wieckowski MR, Giorgi C, Pinton P (2018) Mitochondrial and endoplasmic reticulum calcium homeostasis and cell death. Cell Calcium 69:62–72. https://doi.org/10.1016/j.ceca.2017.05.003
50. Boonrungsiman S, Gentleman E, Carzaniga R, Evans ND, McComb DW, Porter AE, Stevens MM (2012) The role of intracellular calcium phosphate in osteoblast-mediated bone apatite formation. Proc Natl Acad Sci U S A 109:14170–14175. https://doi.org/10.1073/pnas.1208916109
51. Iwayama T, Okada T, Ueda T, Tomita K, Matsumoto S, Takedachi M, Wakisaka S, Noda T, Ogura T, Okano T, Fratzl P, Ogura T, Murakami S (2019) Osteoblastic lysosome plays a central role in mineralization. Science Adv 5:eaax0672. https://doi.org/10.1126/sciadv.aax0672
52. Primaditya V, Coryah FAN, Ariati LIP, Zakiah DWKK, Yuningsih PD, Khotimah H, Ali MM, Riawan W (2020) Effect of Centella asiatica to the glucose transporter 4 and osteocalcin on the rotenonee-induced zebrafish larvae (Danio rerio) stunting model. AIP Conf Proc 2231:040070. https://doi.org/10.1063/5.0002607